Electronic Supplementary Information (ESI)

Self-assembly SnO_2/COF catalysts for improved electro-synthesis of hydrogen peroxide

Guoliang Wang[a], Zhikang Bao[b], Yuanan Li[a], Yabing Wang[a], Xuejiao Cui[a], Haochong Zhong[a], Wenjuan Fang*[a], and Jianguo Wang*[a]

[a] Institute of Industrial Catalysis, State Key Laboratory Breeding Base of Green-Chemical Synthesis Technology, Zhejiang University of Technology.
Hangzhou 310032, China
[b] College of Chemical and Material Engineering, Quzhou University.
Quzhou 324000, China

*Correspondence and requests for materials should be addressed to J.G.W. (email: jgw@zjut.edu.cn).

1. Experimental Procedures

1.1. Chemicals and materials

1,3,5-Triformylphloroglucinol (Tp, 99.5%, Aladdin), p-phenylenediamine (Pa, 99%, Macklin), acetic acid (99.5%, Aladdin), Tin Tetrachloride ($SnCl_4 \cdot 5H_2O$, 99%, Aladdin), Potassium hydroxide (KOH, Macklin, 99.5%), Hydrochloric acid (HCl, Lingfeng Chemical Reagent Co., Ltd, 36%), Sulfuric acid (H_2SO_4, Lingfeng Chemical Reagent Co., Ltd, 99.9%), Ammonia ($NH_3 \cdot H_2O$, Lingfeng Chemical Reagent Co., Ltd, 28%), Dichloromethane (CH_2Cl_2, AR, China National Medicines Co., Ltd), Trichloromethane ($CHCl_3$, AR, China National Medicines Co., Ltd),Potassium titanyl oxalate ($C_4K_2O_9Ti \cdot 2H_2O$, Macklin, 99%), Potassium ferricyanide ($K_3FeC_6N_6$, Macklin, ≥99.5%), Nafion (DuPont), Ethanol (CH_3CH_2OH, Sinopharm Chemical Reagent Co., Ltd, 99.5%), Deionized water (DI, Millipore 18.2 MΩ cm^{-1}), hydrogen peroxide (H_2O_2, Alfa Aesar, 35% w/w), O_2 (99.99%) and N_2 (99.99%) were purchased from Hangzhou Jingong Special Gas Co., Ltd. All reagents are used directly without further purification.

1.2. Synthesis of SnO_2 nanoparticles

SnO_2 was synthesized by a hydrothermal method. Typically, an appropriate amount of $SnCl_4 \cdot 5H_2O$ was dissolved into deionized water to fabricate solution A. Ammonia was added into solution A under continuous stirring until the pH of the solution was 9 . The obtained dispersion was transferred to a Teflon and treated at 120 °C for 12 h before filtration and rinsing with water and ethanol to collect white precipitation (solid B). This solid was washed by deionized water three times and treated by freeze-dried. The resulting white powders were denoted as SnO_2 nanoparticles.[1]

1.3. Synthesis of COF

Tp (200 mg, 0.9517 mmol), Pa (200 mg, 1.849 mmol) and 3 mL acetic acid were dissolved in 150 mL CH_2Cl_2 and 50 mL $CHCl_3$, and the mixture was aging at room temperature for 48 h. The products were harvested by centrifugation and washed with CH_2Cl_2 for twice.[2]

1.4. Synthesis of m-SnO_2/COF

Take 10%SnO_2/COF as an example. After weighing 200 mg of COF, 20 mg of SnO_2 was accurately weighed. Transferring the powder to a mortar, adding a little ethanol (adjust pH to 2 with 1 M hydrochloric acid) for better contact, then powder was ground for about twenty minutes until all the ethanol has evaporated, powder left in the mortar was named 10%SnO_2/COF.

2. Materials characterization

The morphology of the samples was observed by emission scanning electron microscope (FE-SEM) (HITACHI Regulus 8100) at 15 kV acceleration voltage. In order to further observe the submicro-structure of the catalyst, the distribution of related elements was analyzed by 300 kV transmission electron microscope (TEM, Tecnai G2 F30 S-Twin) and energy dispersive spectrometer (EDS, Xplore 80). X-ray diffraction (XRD) was performed on A PANalytical X-pert Pro X-ray diffractometer under the irradiation of CuKa (λ = 1.5418 A) at 40 kV and 40 mA. X-ray photoelectron spectroscopy (XPS) was tested using the Thermo Scientific K-Alpha photoelectron spectrometer. N_2 adsorption/desorption isotherms were measured at -196 °C using the Micromeritics ASAP 2020 system. The UV-visible light absorption spectrum was recorded by Mapada P4. IS50 Fourier transform infrared spectroscopy was performed using KBr particle method (FTIR, Thermo Scientific, USA). The specific surface area was calculated using the Brunauer-Emmett-Taylor (BET) method. The pore size distribution was calculated by Barrett-Joyner-Halenda (BJH) method. A confocal Raman microscope (Alpha300R, WITec GmbH, Germany) with a light source of 514 nm and an integration time of 1 s was used to obtain Raman spectra. The ATR-SEIRAS spectrum was obtained by the Nicolet iS50 Fourier transform infrared spectrometer with a built-in MCT-A detector. Electron spin resonance (ESR) was performed on Bruker EMX-plus.

3. Details for Electrochemical Measurements.

3.1. 2e^- ORR performance measurements

Electrochemical experiments were conducted using an electrochemical workstation (CHI760E) at room temperature. The three-electrode system was constructed with an RRDE (RRDE-3A, ALS Co., Ltd) working electrode, Pt wire counter electrode, and saturated calomel electrode (SCE) reference electrode. The electrocatalyst ink was prepared by mixing 4 mg of

electrocatalyst, 900 μL of absolute ethanol, 100 μL of 0.5% Nafion, followed by ultrasonication for 45 min. 5 μL of the electrocatalyst ink was pipetted and dropped onto the GC disk (0.1256 cm^2) and dried at Infrared lamp to obtain a target electrocatalyst loading of 39.8 μg/cm^2.

The cyclic voltammetry (CV) of oxygen reduction reaction was conducted in O_2-saturated 0.1 M KOH with the potential range of 0-1.2 V (vs. RHE) and scan rate of 5 mV/s. The linear sweep voltammetry (LSV) of oxygen reduction reaction was measured in O_2-saturated 0.1 M KOH using RRDE and CHI760E at the rotation speed of 1600 rpm with the potential range of 0-1.2 V (vs. RHE) and scan rate of 5 mV/s. The H_2O_2 produced on the disk electrode detected by the ring electrode which the potential fixed at 1.29 V (vs. RHE). The H_2O_2 selectivity of the electrocatalysts was calculated the both disc and ring current using the following equations (1) and (2):

$$H_2O_2\% = 200 \times \frac{I_R/N}{I_D + I_R/N} \quad (1)$$

$$n = 4 \times \frac{I_D/N}{I_D + I_R/N} \quad (2)$$

where I_D was disk current, I_R was ring current, and N was current collection coefficient of the Pt ring. N was determined to be 0.4 in our system after calibration using the reversible $[Fe(CN)_6]^{4-/3-}$ redox couple (+0.36 vs. SHE).

3.2. Collection Efficiency of RRDE measurements

Measure of the collection efficiency was performed on the blank RRDE (0.1256 cm^2 of GC disc area, 0.1884 cm^2 of Pt ring area). The Pt ring collection efficiency (N) was determined using the single-electron reversible redox ferrocyanide/ferricyanide system. Specifically, the electrolyte was prepared by dissolving 10 mM of potassium ferricyanide(III) ($K_3[Fe(CN)_6]$, Macklin, 99%) in 0.1 M KOH. It is recommended to purify the electrolyte with Ar gas for at least 30 min prior to measurement in order to eliminate any dissolved O_2 gas. Maintaining an atmosphere of Ar gas into electrolyte during measurements is essential in order to ensure accurate results.

RRDE voltammograms were recorded by performing LSV on the disk from 1.2 V_{RHE} to 0 V_{RHE} at 10 mV/s and different rotation rates (400, 625, 900, 1225, 1600, 2025 and 2500 rpm), meanwhile the ring was held at 1.30 V_{RHE} (Figure. S9). The collection efficiency (N) of RRDE is calculated using the equation (3):

$$N = I_{ring}/I_{disk} \quad (3)$$

where I_{ring} and I_{disk} are the ring and the disk current, respectively. The ferrocyanide reduced on the disk electrode is sent to the Pt ring range due to diffusion, and the voltage applied on the Pt ring will oxide the ferrocyanide to ferricyanide. The current generated is a reflection of the collection efficiency that a platinum ring can provide. When both ferricyanide reduction on the bare GC disk and ferrocyanide oxidation on the Pt ring became diffusion-limited, the N was found to be 0.4 and was independent of the RRDE rotation rate.

3.3. H_2O_2 Faraday efficiency and production measurements

To assess the hydrogen peroxide output (yield), the working electrode employed the following method: the catalyst dispersion, containing a certain amount of Nafion solution, was directly sprayed onto a diffusion layer (Suzhou Saintly, YLS-30T). The entire assembly was used as the working electrode with the aim of obtaining a more pronounced current. The effective area of the experimental setup was 3 × 3 cm. The diffusion layer was cut into small pieces of 3 × 3 cm using scissors as the working area, and the catalyst dispersion was sprayed onto the diffusion layer to create the corresponding cathode. The anode electrode directly utilized commercially available stable metal oxide anode materials (MMO, IrO_2/Ta_2O_5-Ti). The catalyst powder was combined with GDL carbon paper to form the cathode electrode.

During the yield test, the O_2 flow rate was maintained at 10 mL min^{-1}, and the current was set at a fixed value. Every hour, 1 mL of cathode electrolyte was taken as the test sample. Additionally, 1 mL of H_2SO_4 (0.5 M) and 1 mL of $C_4K_2O_9Ti$ (0.05 M) were mixed with the sample. Due to the formation of pro-oxidant, the solution rapidly turned yellow. The concentration of H_2O_2 was ultimately determined through UV-vis technology (λ=400 nm) and a pre-measured standard curve. Faradaic efficiency was calculated using Equation (4):

$$FE\% = \frac{2 \times C \times V \times F}{Q} \times 100\% \quad (4)$$

3.4. Electrochemical active surface area and tafel measurements

Electrochemical capacitance measurements were employed to quantify the electrochemical active surface area (ECSA) of catalysts. Scan rates ranging from 20 to 100 $mV \cdot s^{-1}$ were utilized in order to assess the ECSA. Specially, plotting the cathodic current versus the scanning rate of a

double-layer capacitor yields a linear relationship following the ideal behavior of a capacitor. The electrochemical mass activity of the catalyst was calculated using equations (8) and (9).

$$C_{dl} = \frac{I_C}{v} \tag{5}$$

$$Rf(Roughness\ factor) = \frac{C_{dl}}{C_s} \tag{6}$$

$$ECSA = R_f \times A_{GCE} \tag{7}$$

$$MA = \frac{r_f j_k}{m} \tag{8}$$

$$r_f = \frac{A_{real}}{A_{geo}} \tag{9}$$

I_c represents the average cathodic current, and C_{dl} denotes the double-layer capacitance. The symbol v represents the scan rate. The slope of this line can be utilized to determine C_{dl}. Linear fitting of the resulting curves can be employed to assess the specific capacitance of each catalyst. In addition, the specific capacitance (C_S) of a flat surface is usually 20 - 60 μF cm^{-2}. We used 40 μF cm^{-2} in this work. A_{GCE} is the electrode surface area.In the equations (8) and (9), j_k: Kinetic current density; m: Catalyst loading density on the electrode, mg/cm^2; R_f: Roughness factor; A_{real}: Real surface area of the catalyst, measured from the CV curve (ECSA); A_{geo}: Geometric surface area of the working electrode.

The kinetic current densities (j_k) was obtained by Koutecky-Levich equation (10) and (11):

$$\frac{1}{J} = \frac{1}{J_L} + \frac{1}{J_K} = \frac{1}{B\omega^{1/2}} + \frac{1}{J_K} \tag{10}$$

$$B = 0.2nFC_0D_0^{2/3}V^{-1/6} \tag{11}$$

Where J, J_K and J_L represents the measured current density, the kinetic and diffusion-limiting current densities, ω is the angular velocity, C_0 is the bulk concentration of O_2 (1.2×10^{-6} mol cm^{-3}), D_0 is the diffusion coefficient of O_2 in 0.1 M KOH and 0.5 M Na_2SO_4 (1.9×10^{-5} cm^2 s^{-1}), and V is the kinematic viscosity of the electrolyte (0.01 cm^2 s^{-1}), the number of electrons transferred (n) was obtained by equation (2).

Calculated electrochemical active surface area.

In 0.5 M Na_2SO_4 solution:

$$ECSA_{COF} = \frac{0.21\ mF\ cm^{-2}}{40\ \mu F\ cm^{-2}\ per\ cm^2_{ECSA}} = 5.25\ cm^2_{ECSA}$$

$$ECSA_{SnO_2} = \frac{0.48\ mF\ cm^{-2}}{40\ \mu F\ cm^{-2}\ per\ cm^2_{ECSA}} = 12.00\ cm^2_{ECSA}$$

$$ECSA_{5\%SnO_2/COF} = \frac{0.49\ mF\ cm^{-2}}{40\ \mu F\ cm^{-2}\ per\ cm^2_{ECSA}} = 12.25\ cm^2_{ECSA}$$

$$ECSA_{10\%SnO_2/COF} = \frac{0.66\ mF\ cm^{-2}}{40\ \mu F\ cm^{-2}\ per\ cm^2_{ECSA}} = 16.50\ cm^2_{ECSA}$$

$$ECSA_{15\%SnO_2/COF} = \frac{0.53\ mF\ cm^{-2}}{40\ \mu F\ cm^{-2}\ per\ cm^2_{ECSA}} = 13.25\ cm^2_{ECSA}$$

In 1 M KOH solution:

$$ECSA_{COF} = \frac{0.28\ mF\ cm^{-2}}{40\ \mu F\ cm^{-2}\ per\ cm^2_{ECSA}} = 7.00\ cm^2_{ECSA}$$

$$ECSA_{SnO_2} = \frac{0.48\ mF\ cm^{-2}}{40\ \mu F\ cm^{-2}\ per\ cm^2_{ECSA}} = 12.00\ cm^2_{ECSA}$$

$$ECSA_{5\%SnO_2/COF} = \frac{0.41\ mF\ cm^{-2}}{40\ \mu F\ cm^{-2}\ per\ cm^2_{ECSA}} = 10.25\ cm^2_{ECSA}$$

$$ECSA_{10\%SnO_2/COF} = \frac{0.61\ mF\ cm^{-2}}{40\ \mu F\ cm^{-2}\ per\ cm^2_{ECSA}} = 15.25\ cm^2_{ECSA}$$

$$ECSA_{15\%SnO_2/COF} = \frac{0.43\ mF\ cm^{-2}}{40\ \mu F\ cm^{-2}\ per\ cm^2_{ECSA}} = 10.75\ cm^2_{ECSA}$$

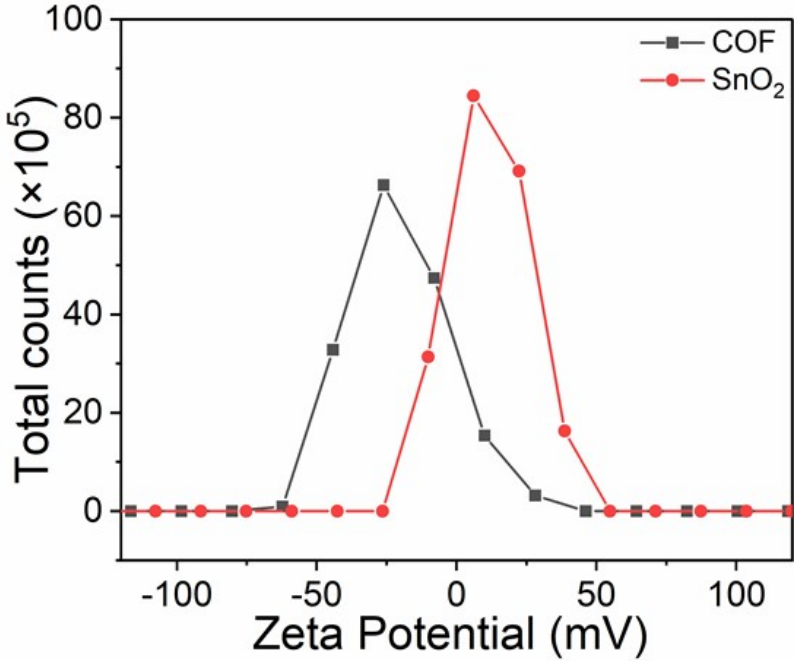

Figure S1. Zeta potentials of SnO_2 and COF (pH = 2).

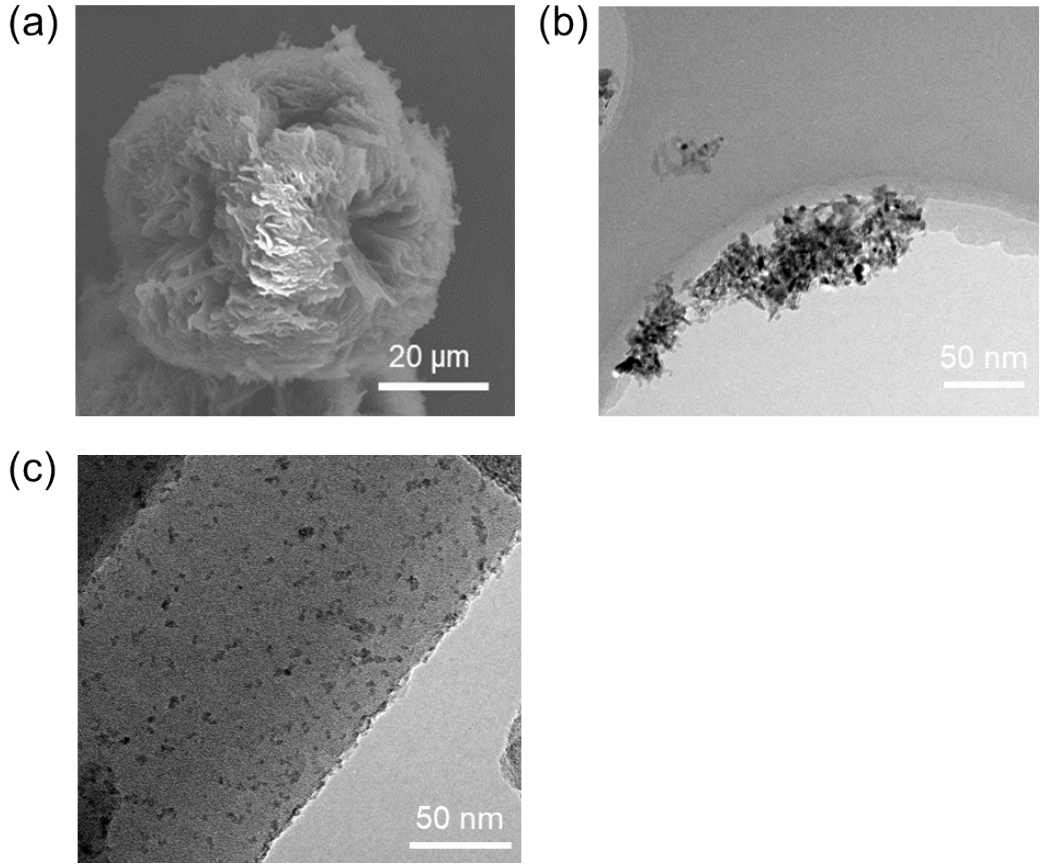

Figure S2. (a) The SEM image of COF, The TEM image of (b) SnO_2 nanoparticles and (c) 10%SnO_2/COF

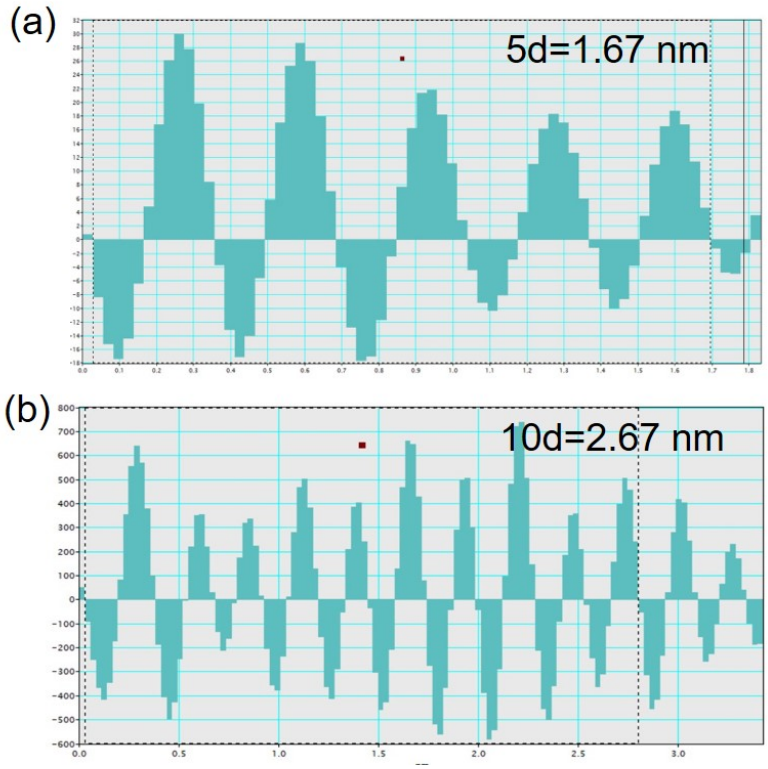

Figure S3. The details about the measurement of lattice fringes belong to (a) SnO_2 (110) and (b) SnO_2 (101) .

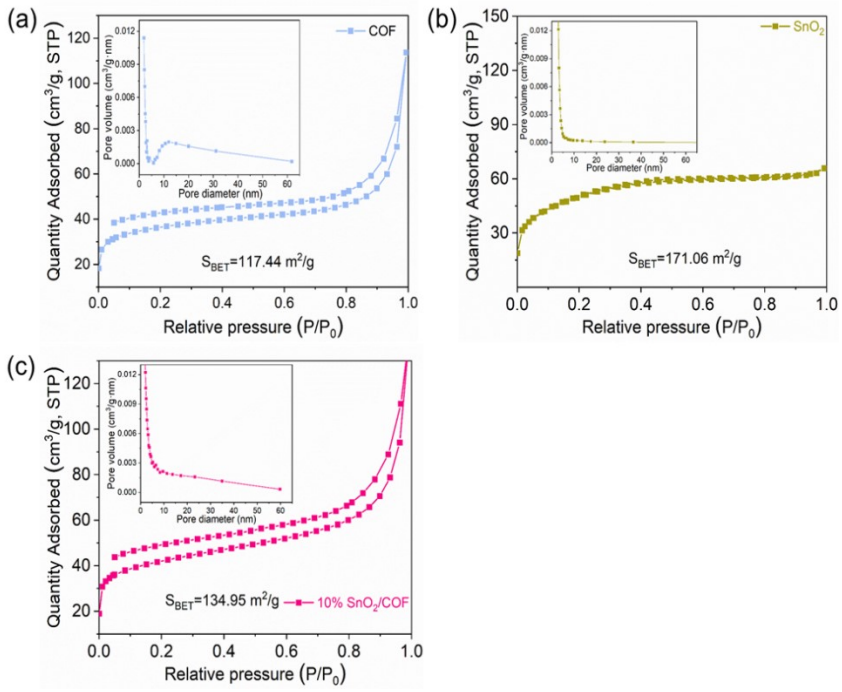

Figure S4. N_2 adsorption–desorption isotherms of (a) COF, (b) SnO_2 and (c) 10% SnO_2/COF. The inset shows the pore volume.

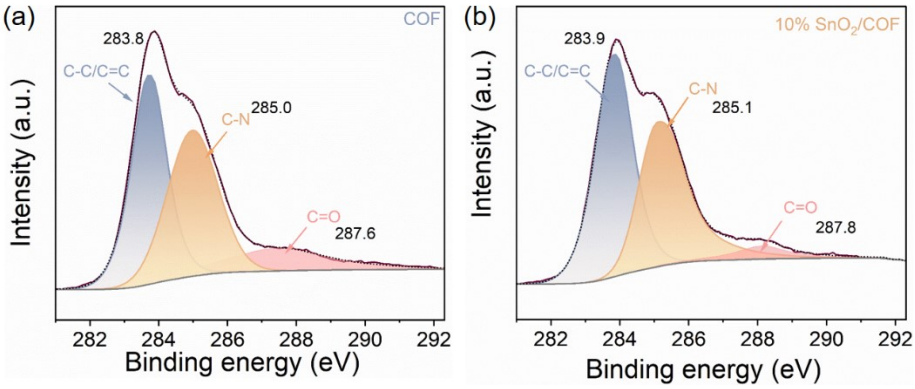

Figure S5. C 1s XPS spectra of (a) COF and (b) 10%SnO_2/COF.

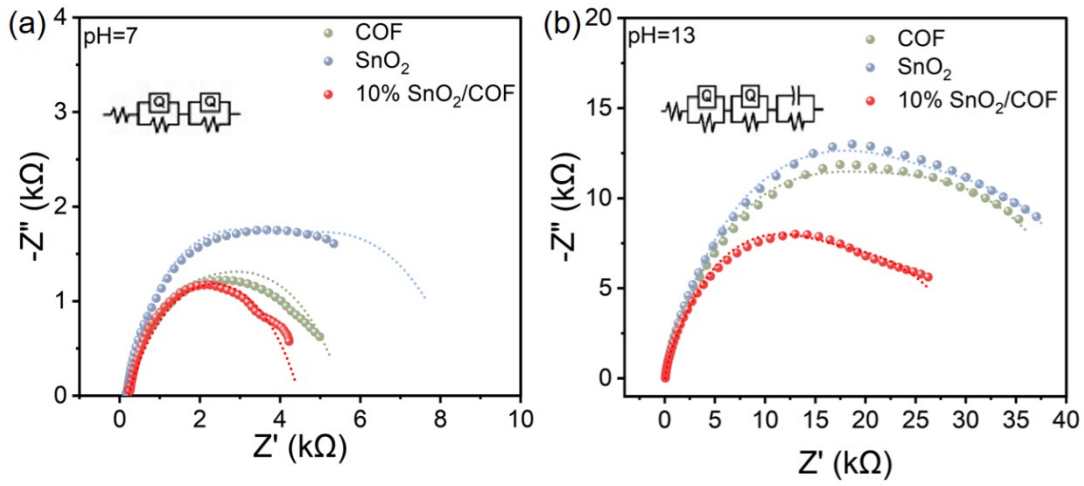

Figure S6. EIS Nyquist plots and fitting results of COF, SnO_2 and 10% SnO_2/COF at (a) 0.5 M Na_2SO_4 solution (pH=7) and (b) 0.1 M KOH solution (pH=13).

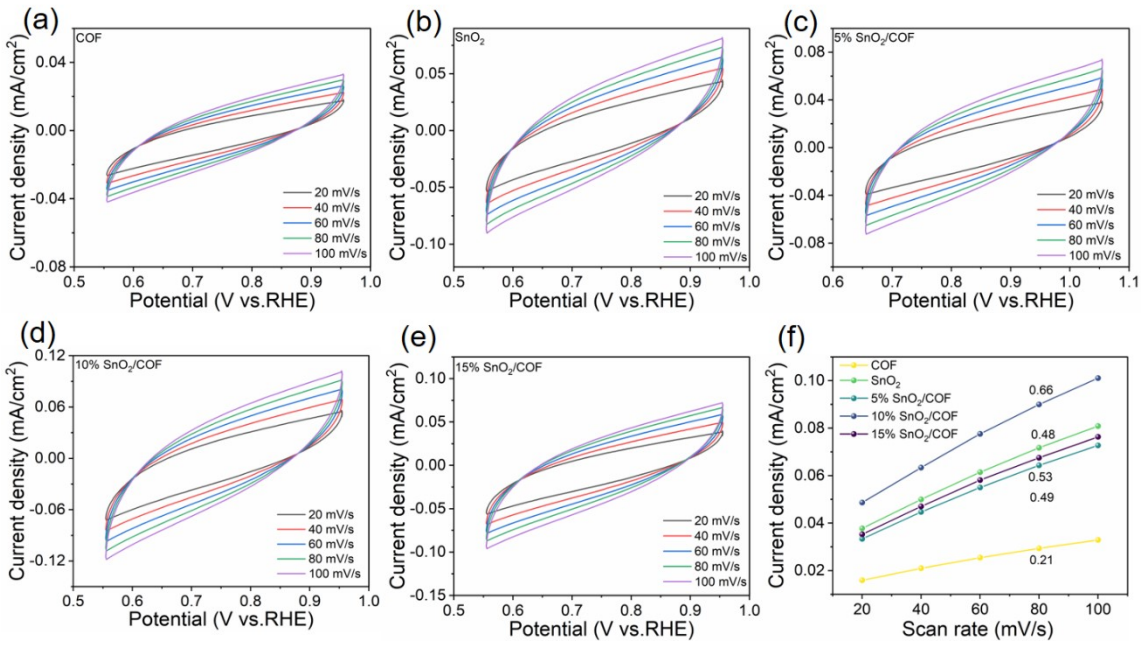

Figure S7. CV curves in 0.5 M Na_2SO_4 solution (pH=7) of (a) COF, (b) SnO_2, (c) 5% SnO_2/COF, (d) 10% SnO_2/COF, (e) 15% SnO_2/COF with various scan rates for $2e^-$ ORR; (f) Capacitive currents as a function of scan rates with various rates from 20 to 100 mV/s of virous catalysis.

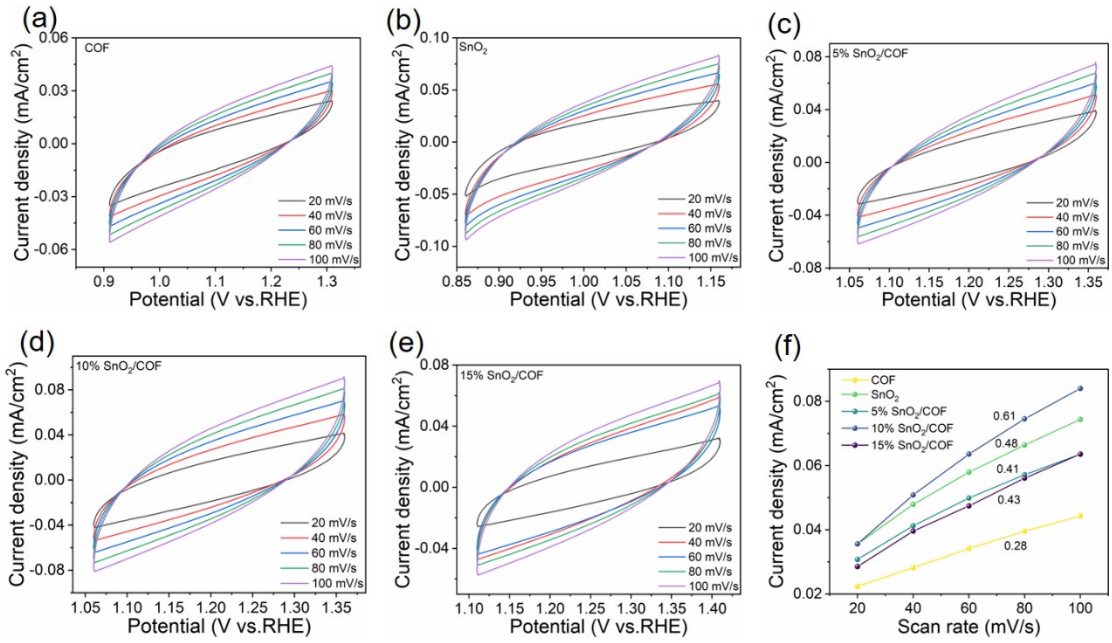

Figure S8. CV curves in 0.1 M KOH solution (pH=13) of (a) COF, (b) SnO_2, (c) 5% SnO_2/COF, (d) 10% SnO_2/COF, (e) 15% SnO_2/COF with various scan rates for $2e^-$ ORR; (f) Capacitive currents as a function of scan rates with various rates from 20 to 100 mV/s of virous catalysis.

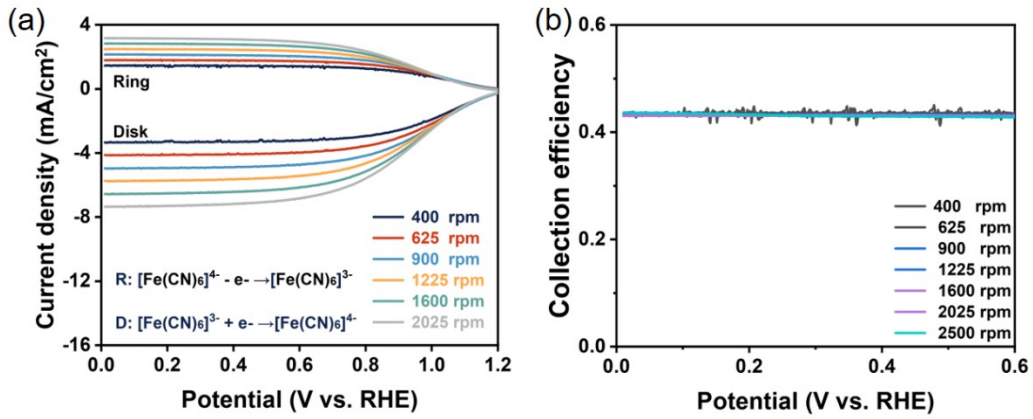

Figure S9. (a) LSV at different rotating speeds. (b) the corresponding collection efficiency of RRDE voltammograms as a function of the potential.

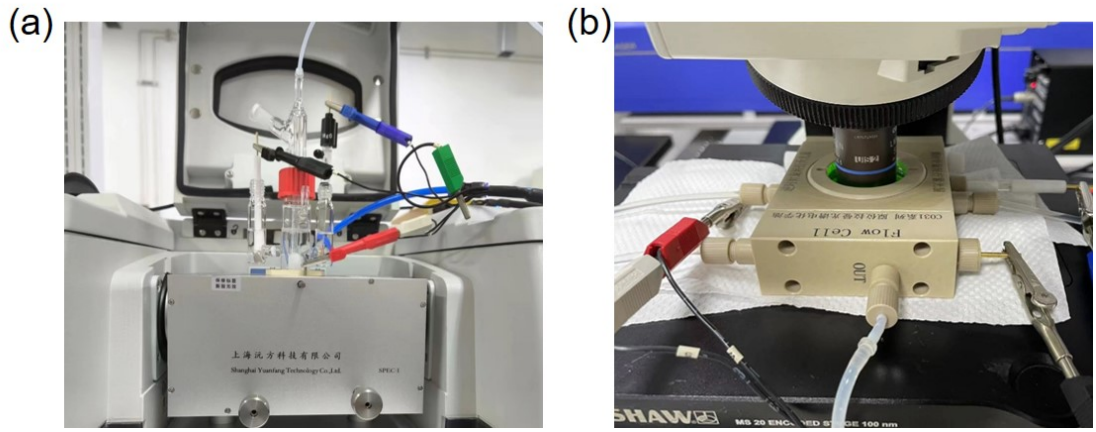

Figure S10. (a) Diagram of devices placement during in-situ Raman measurement；(b) Diagram of devices placement during in-situ ATR-SEIRAS.

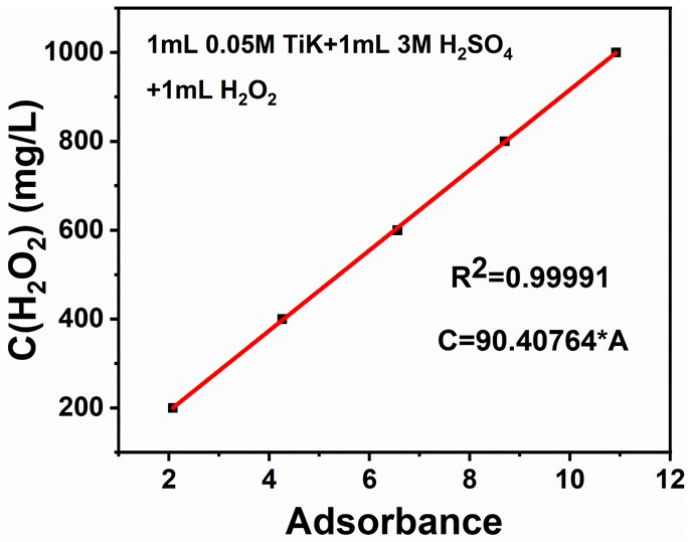

Figure S11. H_2O_2 concentration-absorbance standard curve.

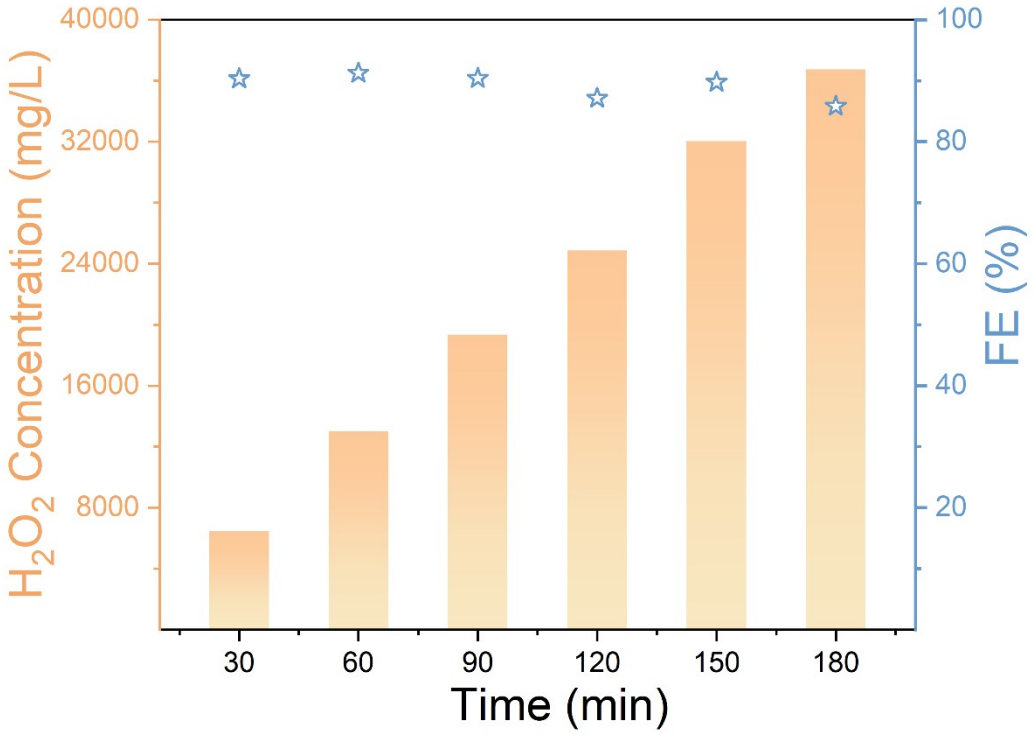

Figure S12. Time depending H_2O_2 concentration and FE in 0.1 M KOH solution with flow-cell.

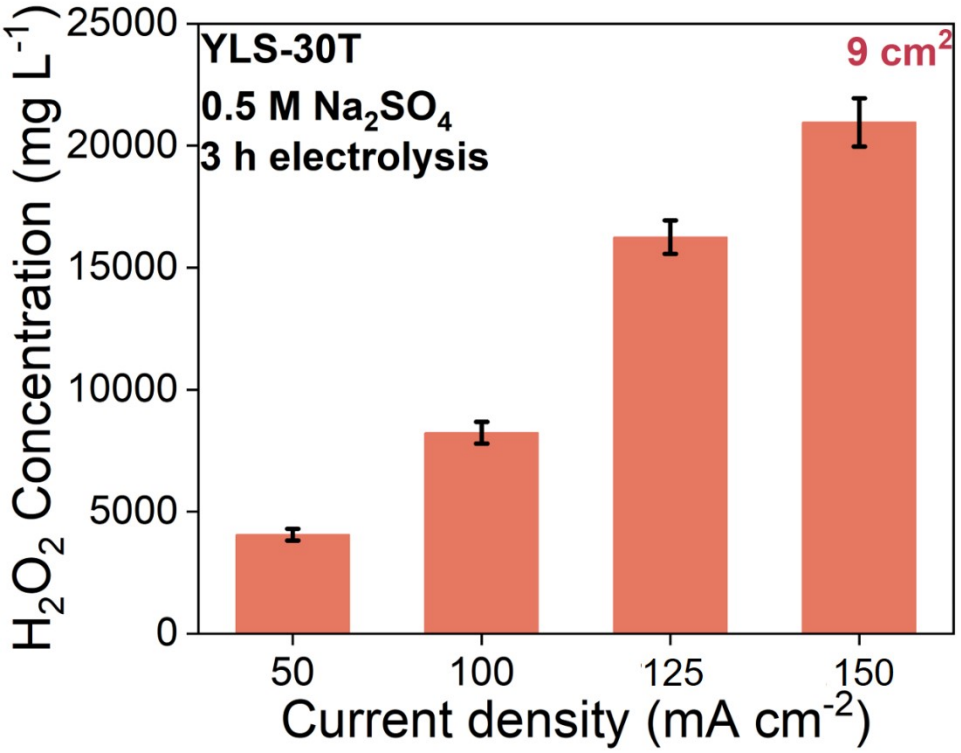

Figure S13. H_2O_2 concentration of carbon paper at different current densities (50, 100, 150, and 200 mA/cm^2) in 0.5 M Na_2SO_4 soulution with flow-cell.

Catalysts	H_2O_2 selectivity (%)*	H_2O_2 yield (mmol g^{-1} h^{-1})	FE (%)#	Electrolyzer	H_2O_2 concentration (wt.%)	Refs.
SnO_2/COF	**95.8**	**19607**	**85**	**Flow Cell**	**3.5 (3 h)**	**This work**
ZnO-v	98.4	3658	98.1	Flow Cell	/	3
Co SACs	95.6	4500	95	Flow Cell	/	4
h-SnO_2	99.99	3885.26	/	Flow Cell	0.0011 (20 h)	5
a-$PdSe_2$ NPs/C	90	2242.1	/	Flow Cell	0.1 (2 h)	6
PtP_2 NCs	98.5	2825	78.8	PEMFC	3 (65 h)	7
In SAs/NSBC	95	6710	80	PEMFC	/	8

*The data are from RRDE setup. #The data are obtained from electrolyzer.

Table S1. Comparative analysis of state-of-the-art metal-based electrocatalysis for $2e^-$ ORR H_2O_2 production in neutral electrolyte.

Catalysts	H_2O_2 selectivity (%)*	H_2O_2 yield (mmol g^{-1} h^{-1})	FE (%)#	Electrolyzer	H_2O_2 concentration (wt.%)	Refs.
SnO_2/COF	**98.5**	**20016**	**85.8**	**Flow Cell**	**3.5 (3 h)**	**This work**
$Fe_{SA-NS/C-700}$	92	4950	91.4	Flow Cell	5.8 (30 h)	9
Co-N-C	80	4330	52	Flow Cell	/	10
Ni/C-4	95	906	95	Flow Cell	0.051 (100 h)	11
CSH-600	96	0.6924	93.1	Flow Cell	/	12
Co-SCD-2	95.2	26780	85	Flow Cell	/	13
ZnCo-ZIFs	99	4350	95	Flow Cell	2.7 (2 h)	14
CoPc-OCNT	99	11527	91	Flow Cell	3.7 (/)	15
Mn-NO-C_H	98.5	15100	~100	Flow Cell	4.84 (50 h)	16

*The data from RRDE setup. #The data from electrolyzer.

Table S2. Comparative analysis of state-of-the-art metal-based electrocatalysis for $2e^-$ ORR H_2O_2 production in basic electrolyte.

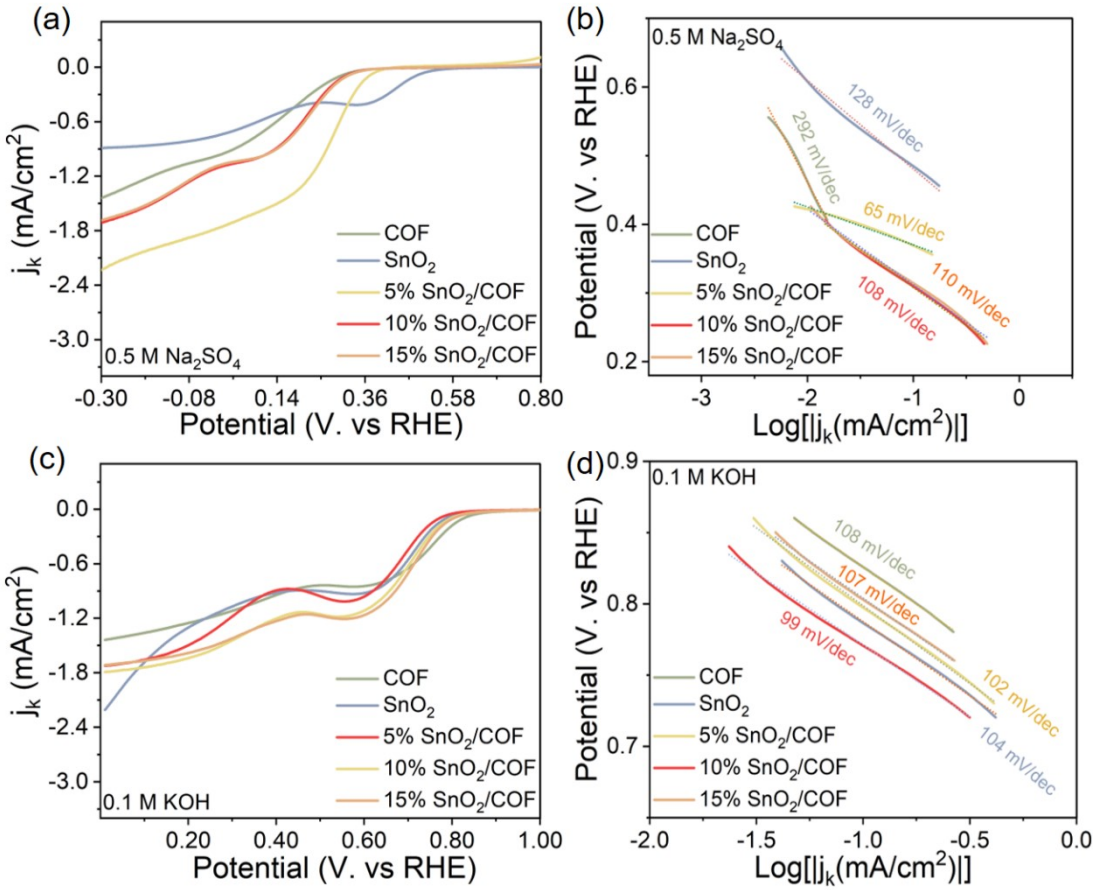

Figure S14. The kinetic current densities of different electrocatalyst in (a) 0.5 M Na_2SO_4 and (c) 0.1 M KOH. The tafel slopes for different electrocatalyst in (b) 0.5 M Na_2SO_4 and (d) 0.1 M KOH.

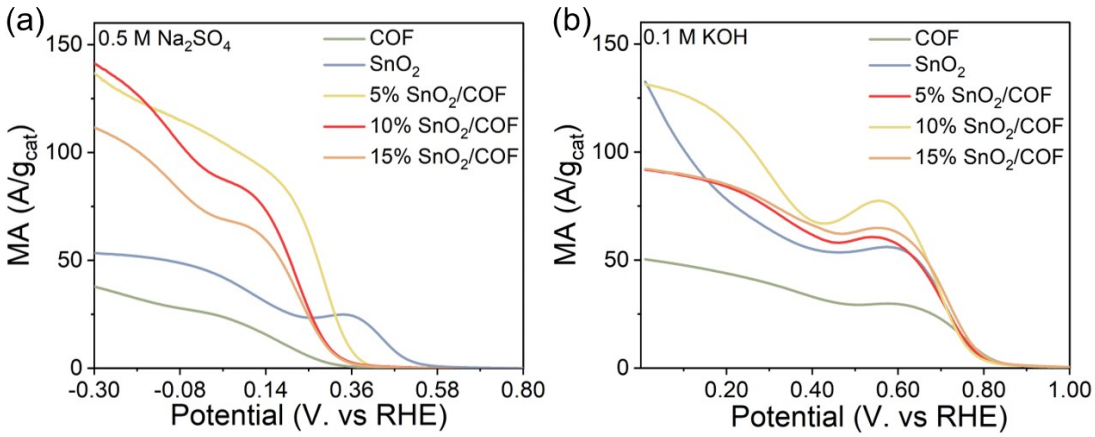

Figure S15. The mass activity of different electrocatalyst in (a) 0.5 M Na_2SO_4 and (b) .0.1 M KOH.

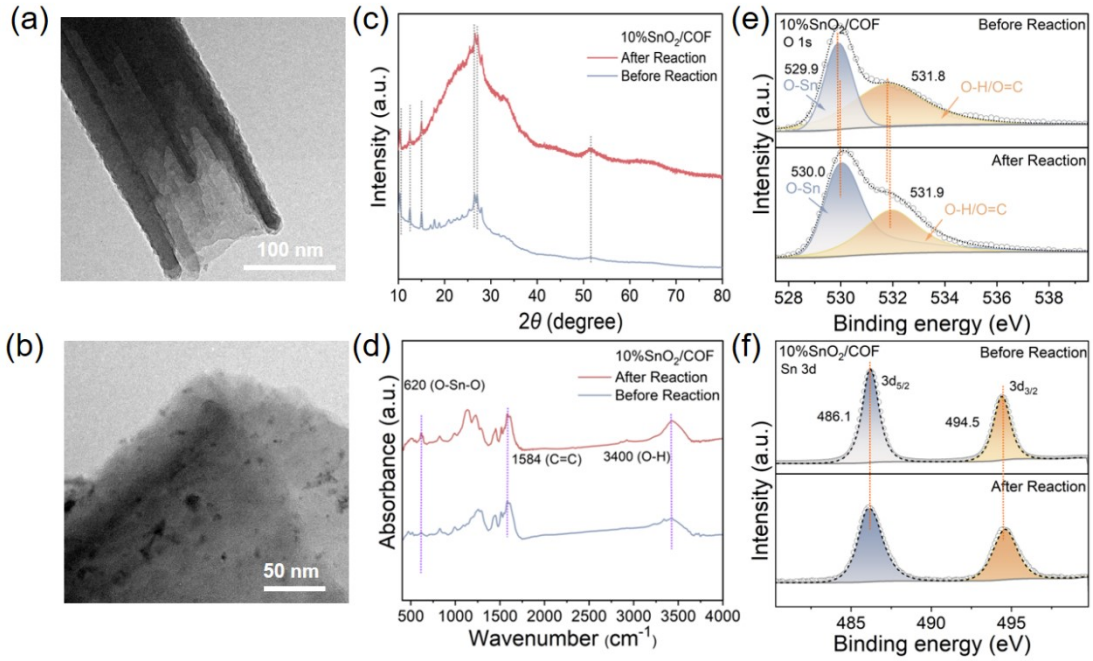

Figure S16. (a,b) TEM images of the catalyst after 20 cycles; (c) XRD, (d) FT-IR, (e) O 1s, and (f) Sn 3d spectra before and after 20 cycles.

Reference

1. M. Ahamed, M. J. Akhtar, M. A. M. Khan and H. A. Alhadlaq, *Int J Nanomedicine*, 2021, **16**, 89-104.
2. Y. Shi, S. Liu, Z. Zhang, Y. Liu and M. Pang, *Chemical Communications*, 2019, **55**, 14315-14318.
3. S. Ding, Y. Zhang, F. Lou, M. Li, Q. Huang, K. Yang, B. Xia, C. Tang, J. Duan, M. Antonietti and S. Chen, *Materials Today Energy*, 2023, **38**, 101430.
4. Q. Zhao, Y. Wang, W. H. Lai, F. Xiao, Y. Lyu, C. Liao and M. Shao, *Energy & Environmental Science*, 2021, **14**, 5444-5456.
5. Y. Zhang, M. Wang, W. Zhu, M. Fang, M. Ma, F. Liao, H. Yang, T. Cheng, C.-W. Pao, Y.-C. Chang, Z. Hu, Q. Shao, M. Shao and Z. Kang, *Angew. Chem., Int. Ed.*, 2023, **62**, e202218924.
6. Z. Yu, S. Lv, Q. Yao, N. Fang, Y. Xu, Q. Shao, C.-W. Pao, J.-F. Lee, G. Li, L. Yang and X. Huang, *Advanced Materials*, 2022, **35**, 2208101.
7. H. Li, P. Wen, D. S. Itanze, Z. D. Hood, S. Adhikari, C. Lu, X. Ma, C. Dun, L. Jiang, D. L. Carroll, Y. Qiu and S. M. Geyer, *Nature Communications*, 2020, **11**, 3928.
8. E. Zhang, L. Tao, J. An, J. Zhang, L. Meng, X. Zheng, Y. Wang, N. Li, S. Du, J. Zhang, D. Wang and Y. Li, *Angewandte Chemie International Edition*, 2022, **61**, e202117347.
9. Y. Li, J. Chen, Y. Ji, Z. Zhao, W. Cui, X. Sang, Y. Cheng, B. Yang, Z. Li, Q. Zhang, L. Lei, Z. Wen, L. Dai and Y. Hou, *Angewandte Chemie International Edition*, 2023, **62**, e202306491.
10. Y. Sun, L. Silvioli, N. R. Sahraie, W. Ju, J. Li, A. Zitolo, S. Li, A. Bagger, L. Arnarson and X. Wang, *Journal of the American Chemical Society*, 2019, **141**, 12372-12381.
11. H. Shen, L. Pan, T. Thomas, J. Wang, X. Guo, Y. Zhu, K. Luo, S. Du, H. Guo and G. J. Hutchings, *Cell Reports Physical Science*, 2020, **1**.
12. G. Wei, Y. Li, X. Liu, J. Huang, M. Liu, D. Luan, S. Gao and X. W. Lou, *Angewandte Chemie*, 2023, **135**, e202313914.
13. D. Qi, J. Xu, Y. Zhou, H. Zhang, J. Shi, K. He, Y. Yuan, J. Luo, S. Wang and Y. Wang, *Angewandte Chemie*, 2023, **135**, e202307355.
14. C. Zhang, L. Yuan, C. Liu, Z. Li, Y. Zou, X. Zhang, Y. Zhang, Z. Zhang, G. Wei and C. Yu, *Journal of the American Chemical Society*, 2023, **145**, 7791-7799.
15. P. Cao, X. Quan, X. Nie, K. Zhao, Y. Liu, S. Chen, H. Yu and J. G. Chen, *Nature Communications*, 2023, **14**, 172.
16. L. Y. Dong, J. S. Wang, T. Y. Li, T. Wu, X. Hu, Y. T. Wu, M. Y. Zhu, G. P. Hao and A. H. Lu, *Angewandte Chemie International Edition*, 2024, **63**, e202317660.